International Journal of Rock Mechanics and Mining Sciences 121 (2019) 104046

Contents lists available at ScienceDirect

International Journal of Rock Mechanics and Mining Sciences

journal homepage: www.elsevier.com/locate/ijrmms

A new apparatus for the concurrent measurement of friction and permeability evolution in fault gouge

Ziyan Li*, Derek Elsworth, Chaoyi Wang, Kyungjae Im

Department of Energy and Mineral Engineering, The Pennsylvania State University, University Park, PA, USA

A B S T R A C T

We introduce a new miniature double direct shear (mini-DDS) apparatus, housed within a standard-triaxial (TEMCO) pressure vessel, capable of concurrently measuring the evolution of frictional strength, stability, healing and along-fault permeability under *in situ* conditions of stress and temperature. The apparatus accommodates gouge samples (25 mm × 32 mm) and intact rock samples with confining and shear stresses and pore pressures up to ~26 MPa. Permeability may be measured with applied flow rates ranging from 1.67×10^{-11} to 3.6×10^{-6} m^3/s to a flow accuracy of 0.5% representing a lower bound of permeability > 2.2×10^{-18} m^2. Sliding velocities are in the range 0.1 μm/s to 0.67 cm/s with a frame stiffness of 0.067 kN/μm. We describe protocols and procedures for calibration and experiments and note the potential of the apparatus for both rapid and extended-duration measurements of friction-permeability evolution and healing. The apparatus returns measurements of friction and stability of reference materials of F110 quartz consistent with the literature while additionally allowing the concurrent measurement of permeability. Permeability of F110 quartz evolves in slide-hold-slide (SHS) experiments with increases during holds and decreases during subsequent slides. These observations are consistent with grain crushing and resultant wear products that reduce that permeability by clogging during slides with unclogging of the major fluid channels occurring during shearing.

1. Introduction

Fault gouge is unconsolidated, granular wear materials that are developed by shearing and grinding through relative movement of slipping wall rocks. Measurement of the frictional (frictional strength, stability, and healing behavior) and hydrologic properties (permeability, pore pressure) provide fundamental characteristics to predict fault zone stability and subsurface fluid migration. Fluid overpressures may lubricate the fault and reduce the effective normal stress that locks the fault, promoting slip. This overpressure may result from thermal pressurization due to shear heating, commonly seen in the natural systems,[1–3] or as a result of fluid injection from anthropogenic activities, such as waste water disposal, CO_2 sequestration, hydraulic fracturing, and enhanced geothermal simulation.[4–10] Whether the triggered/induced slip is seismic or aseismic depends largely on the frictional properties of the fault gouge based on rate-and state friction.[11,12] In particular, if the fault is velocity strengthening, where the steady-state frictional resistance increases with sliding velocity, fault slip will result in stable sliding or aseismic fault creep; conversely, velocity weakening may favor unstable, stick-slip behavior associated with earthquake nucleation. The slip behavior of a fault will also attribute rate-dependent properties to permeability.[13,14] It is therefore crucial to understand frictional behavior of fault gouge coupled with hydrological response since these two aspects of faults are intimately related and cannot be considered in isolation.

Many previous studies have focused on characterizing the influence of mineralogical composition of gouge on shear strength, frictional stability and permeability evolution. These properties must be measured simultaneously as permeability is a clear function of shear strain. Much work has shown that clay-rich fault gouges incorporate weak minerals with a coefficient of friction < 0.5 that impart a velocity strengthening response during slip. Even small increases in clay concentrations can dramatically reduce the permeability of fault gouge, possibly reaching four orders of magnitude, as clay content increases from 0 to 50% under otherwise identical conditions[15,16]. However, our understanding of systematic interrelationships between fault strength, stability and permeability remains limited. Specifically, is there a correlation between frictional weakness and permeability? Does permeability evolution vary due to frictional response (velocity strengthening/weakening)? Can different frictional responses be predicted from permeability evolution?

In order to answer these questions, we first develop a new experimental method that can concurrently measure frictional and hydrological properties of fault gouge. This method is inspired by stiffer and more cumbersome large-scale double direct shear apparatuses,[17–20] but where the pressure vessel now enables essentially routine measurement of hydrological properties. We have developed and report a double direct shear configuration housed within a triaxial pressure vessel

* Corresponding author.
E-mail address: zkl5075@psu.edu (Z. Li).

https://doi.org/10.1016/j.ijrmms.2019.06.005
Received 5 December 2018; Received in revised form 21 May 2019; Accepted 1 June 2019

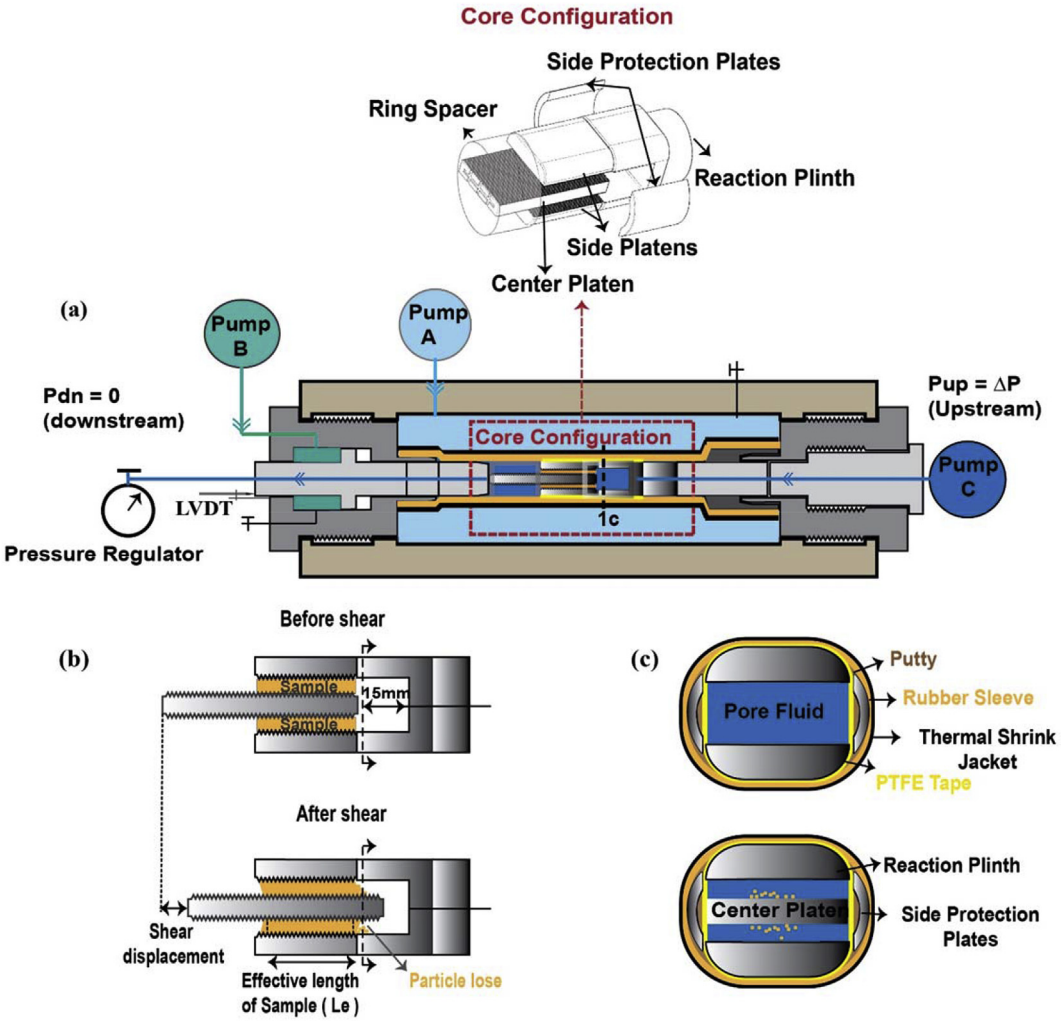

Fig. 1. Schematic diagram of apparatus: (a) Experimental arrangement for measurement of frictional and transport properties with detailed 3D view of core configuration. (b) Double direct shear configuration before/after shear with concept of effective length (L_e). (c) Cross-sectional view of (b) with an illustration of the jacketing system.

(TEMCO), where frictional and hydraulic properties can be measured concurrently with independent application of confining pressure, shear stress, and pore pressure. With such an apparatus, we are able to apply loading on gouge samples and to allow both rapid and long-term experimentation at high resolution. In this work, we describe the design of this new apparatus in detail and present extensive verification experiments to define the fidelity, reproducibility and reliability of parameters measured with the apparatus. We also include a case study using the reference material (F110 quartz) to define the coupled frictional and hydrological properties though velocity-stepping and SHS tests coupled to permeability measurements.

2. Apparatus design

The new miniature double direct shear (mini-DDS) configuration can be run within the TEMCO simple-triaxial core holder by appropriately miniaturizing the core configuration (Fig. 1a). The apparatus consists of four major components: the reaction plinth, shear platens (one center platen and two side platens), side protection plates and ring spacer, all of which are fabricated from stainless steel. The center platen (25.4 mm × 50.8 mm × 6.35 mm) and two side platens (25.4 mm × 31.75 mm × 5.08 mm) constitute the basic double direct shear geometry, and they are all sawtooth-grooved to aid shear coupling with the sample. The reaction plinth is a U-shaped platen that holds the side plates static as the central shear plate is able to penetrate inside this reaction plinth to a maximum shear displacement of 15 mm. This corresponds to the maximum axial length of the void space interior to the reaction plinth, as shown in Fig. 1b. This U-shaped structure (void space) leaves sufficient space for the potential misalignment of the center platen and loss of particles during shearing. However, high confining stress acting on this structure will readily result in the penetration of the confining fluid. Therefore, side protection plates are fixed along the reaction plinth. For the same reason, a ring spacer is attached to the extended part of center platen to increase the average radius of the core configuration so that the confining stress can be distributed uniformly.

We prepare sample layers to a uniform initial thickness using a precision leveling jig, surrounding the perimeter of the side blocks with a flexible adhesive membrane. We then wrap Teflon tape around the U-shaped reaction plinth, preparing the sample and piston together, and attach the twin protection plates. This entire assembly is placed inside a rubber sleeve that is further sealed within a heat-shrink jacket to isolate the sample from the confining fluid. The piston and the connected center (shear) platen can then move inside of the Latex sleeve with all other parts of the core configuration fixed. The shear platen runs into the U-shape platen as the shear displacement is incremented and is guarded within the side protection plates. This entire assembly is then placed inside the TEMCO vessel as shown in Fig. 1a. The uniform

confining stress ($S_2 = S_3$) is applied through Pump A using load-feedback servo control. Constant upstream reservoir pressure or constant flow rate can be applied though Pump C. Downstream reservoir pressure is set at atmospheric pressure. After the sample is saturated with de-ionized water, shear stress is applied by driving the axial/longitudinal piston to displace the center shear platen relative to the flanking side platens and thereby shear the sample layers. Shear is either in prescribed constant load-point velocity or measured force mode control (Pump B). All three pumps, each with a capacity of 507 cm^3, provide precise, predictable flow at flow rates from sub-microliter to 3.6×10^{-6} m^3/s with a flow accuracy of 0.5% of the set point, and pressure control from 70 kPa to 25.8 MPa with pressure accuracy of 0.5% FS. Displacement of the horizontal piston is measured exterior to the TEMCO end cap using a Linear Variable Differential Transformer (LVDT) to a precision of 0.1 μm.

3. Machine calibration and verification

To better understand the fidelity and resolution of friction and permeability measurements made with the mini-DDS configuration within the TEMCO vessel, we first calibrate out machine and jacket stiffnesses. We then measure friction, the velocity dependence of friction, then healing properties of reference materials F110 (99% of quartz) to validate the new DDS against standard measurements. Finally, we characterize permeability response concurrently with friction measurements during SHS experiments.

3.1. Machine stiffness

Machine stiffness reflects the elastic interaction between specimen and testing machine. To measure the machine stiffness, we place an equal length of rigid steel cylinder instead of core (see configuration in Fig. 1) inside the TEMCO vessel and assume that the strain of the cylinder can be ignored.

In this measurement, three load-unload cycles are conducted in succession, as shown in Fig. 2a. The shear load (longitudinal piston) is incremented in steps of 0.25 kN, with each step held for 30 s. After reaching the maximum horizontal load, the shear stress is decremented on the same schedule. Applied stresses and displacements measured by LVDT are correlated to yield machine stiffness (Fig. 2b). The axial displacement increases monotonically and near-linearly with time, implying constant stiffness (average stiffness ~0.067 kN/μm) in loading. The unloading shows slight hysteresis but with similar stiffness.

3.2. Jacket stiffness/resistance

The jacket retains the integrity of the core configuration inside the TEMCO vessel, isolates the sample from the confining fluid and also contains the interior fluid saturant, allowing the measurement of permeability. Thus, the jacket is an essential feature of the apparatus, but higher degrees of security with more cumbersome jackets result in elevated resistance and larger required corrections for jacket/membrane resisting force. Jacket resistance is defined as the extensile force of the latex sleeve when it is being stretched as center platen slides in shear under confining stress. An analysis of the shear platen system is presented in Fig. 3a, where a normal force is applied perpendicular to the side-platens and a shear force is applied longitudinally advance the center platen. Jacket resistance is applied on the surface of the shear platen in the opposite direction to the shear motion. Additionally, friction between the sample and center platen during shearing, defined as the true friction of the sample, also opposes the shear motion. Therefore, force balance of this system in either static or constant velocity modes can be described as

$$F_s = F_j + 2f_s \quad (1)$$

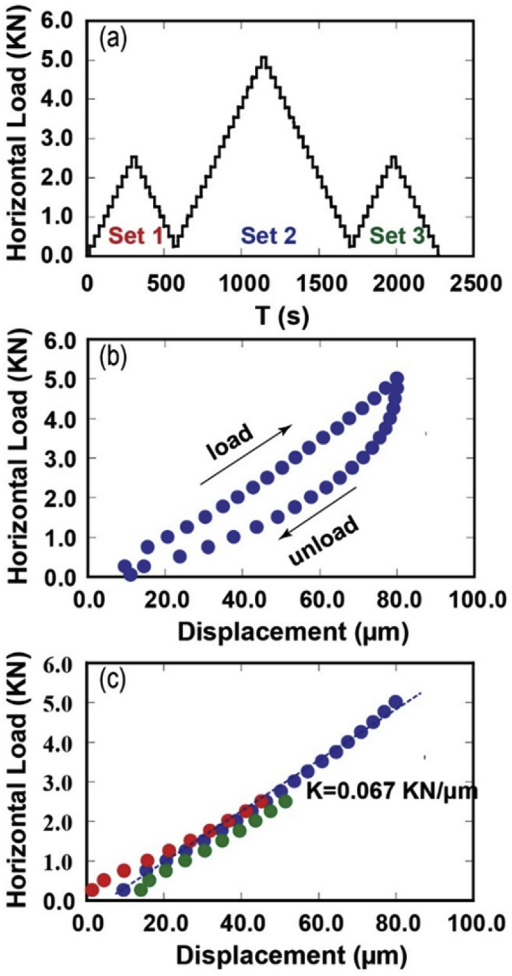

Fig. 2. Measurement of machine stiffness: (a) Experimental procedure adopted to evaluate the stiffness. (b) Illustrative figure of horizontal stiffness for experimental set 2. (c) Horizontal stiffness recovered from three tests.

where F_s [N] is shear force, F_j [N] is the jacket resistance, and f_s [N] is the true friction of the sample, with the coefficient of 2 representing the dual shear components from the two platens.

We use lubricated polished steel platens in lieu of the sample (Fig. 3b) to minimize of sample friction (f_s in eqn. (1) is minimized and assumed to be zero) Therefore, jacket resistance is then recovered from the measured shear force when the shear platen is sliding at constant velocity.

An illustrative example (Exp No. 1) under a confining stress of 2 MPa is shown in Fig. 4a. It indicates that the velocity (blue) of the shear platen first jumps upon initiation ($V = 0$) and then slowly stabilizes to a constant applied velocity of 10 μm/s at ~4000 μm. The jacket resistance can be recovered from the measured shear load (see Fig. 3). Jacket resistance increases as shear displacement accumulates, and the slope of the resistance-displacement curve remains constant with this slope representing jacket stiffness. This parameter is related to confining stress in addition to shear displacement as a higher confining stress inhibits relative slip between the center platen and the latex sleeve. A series of constant velocity sliding experiments are then completed under different confining stresses to measure jacket stiffness as shown in Table 1.

It is shown in Fig. 4b that jacket stiffnesses at different confining stresses (2–10 MPa) are linearly-fit to

$$K_j = 9 \times 10^{-6}\sigma + 6 \times 10^{-8} \quad (2)$$

where K_j [kN/μm] is jacket stiffness, and σ [MPa] is confining stress.

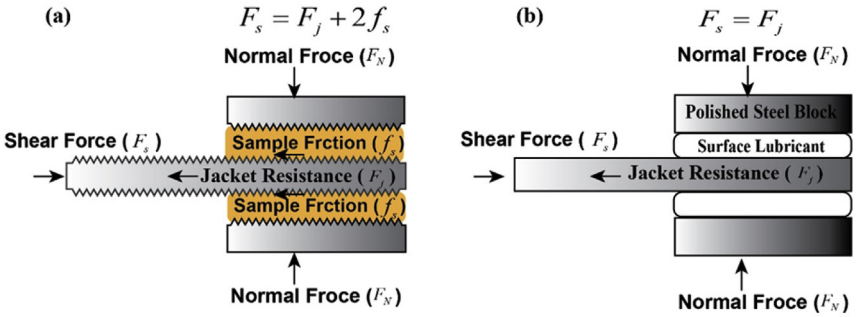

Fig. 3. (a) Force components used in the analysis for the evaluation of frictional and hydraulic properties. (b) Force components defining jacket compliance.

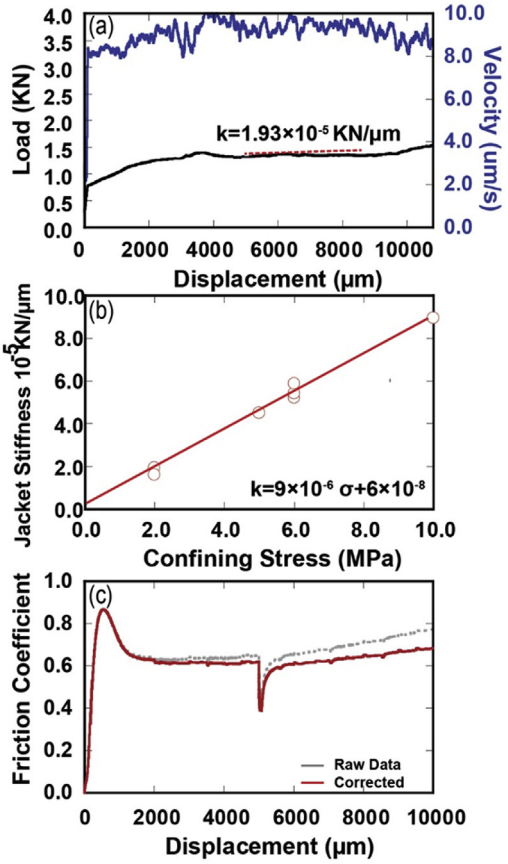

Fig. 4. Jacket stiffness calibration: (a) Load-displacement curve identifying jacket stiffness at a confining stress of 2 MPa. (b) Relationship between jacket stiffness and confining stress. (c) Friction coefficient recovered both with and without corrections for jacket stiffness.

Table 1
Experimental parameters and results of jacket stiffness measurement.

Exp No.	confining pressure (MPa)	shear velocity μm/s	Stiffness KN/μm
1	2	10	1.93E-05
2	2	10	1.62E-05
3	5	10	4.50E-05
4	6	10	5.20E-05
5	6	10	5.41E-05
6	6	10	5.87E-05
7	10	10	8.94E-05

This relationship is based on laboratory observations and can be applied to estimate jacket stiffness as a function of confining stresses between 0 and 10 MPa.

In laboratory friction experiments, friction coefficient is usually recovered from the ratios of shear force to normal force as

$$\mu = \frac{F_s}{2F_N} \tag{3}$$

where F_s [N] is shear force and is recovered from the pump fluid pressure acting on the piston area, as

$$F_s = P_B \times A_{Piston} \tag{4}$$

where P_B [Pa] is the pressure provided by Pump B and A_{Piston} [m^2] is the piston area. F_N [N] is normal force and depends on the relative stress applied to the sample, as

$$F_N = (P_c - P_p) \times L_e \times W \tag{5}$$

where P_c [Pa] is confining pressure, P_p [Pa] is pore pressure, and L_e [m] and W [m] represent the effective length (Fig. 1b) and width of the gouge sample. The frictional coefficient can then be defined as

$$\mu = \frac{P_B \times A_{Piston}}{2(P_c - P_p) \times L_e \times W} \tag{6}$$

If we take jacket stiffness into consideration, the frictional coefficient can be expressed as

$$\mu = \frac{F_s - F_j}{F_N} = \frac{P_B \times A_{Piston} - K_j \times D}{2(P_c - P_p) \times L_e \times W} \tag{7}$$

Finally, we illustrate the importance of the jacket resistance correction (Fig. 4c; data from Table 2) where the correction is or is not applied. As anticipated, the error grows with increased force applied as the jacket stretches at larger shear offsets. This correction enables correction for spurious observations that might otherwise be interpreted as long-term strengthening of the sample.

3.3. Frictional properties

We examine the response of F110 quartz sand to test the fidelity of friction measurements recovered from the mini-DDS. We shear-in the sample at a confining stress of 2 MPa and at a constant load-point velocity of 10 μm/s to steady state and then conduct velocity-stepping (VS) experiments with a repetitive velocity schedule of 1-3-10 μm/s. We then increase the confining pressure to 6 MPa and repeat the velocity step schedule.

It is apparent that the F110 is frictionally strong ($\mu > 0.5$), and exhibits a similar behavior in the frictional strength-displacement curves under both 2 and 6 MPa confining pressure. That is, that after reaching steady state friction at a constant load point shear velocity (~10 μm/s), each velocity step elicits a peak strength that returns to a residual magnitude for confining stresses less than 2 MPa and 6 MPa. Details are given in Table 2.

A single velocity step on F110 is magnified in Fig. 5b for consideration as "representative" behavior. When the velocity changes from V_0 to V ($V_0 < V$), the friction coefficient builds to a peak and then returns to a new steady state. The instantaneous change in friction

Table 2
Schedule of experimental conditions for frictional and hydraulic properties tests.

Exp No.	sample	state	Tests	confining stress (MPa)	pore pressure (MPa)	Velocity (μm/s)
9	F110	dry	stability	2, 6	–	1,3,10
10	F110	water saturated	stability, healing	5	0.3	1,3,10
11	F110	water saturated	stability, healing	5	0.3	1,3,10

coefficient is defined as the direct effect, denoted as a, with the decay to a new residual friction representing the evolution effect, b. If frictional strength increases with increasing sliding velocity, it indicates velocity-strengthening behavior (a-$b > 0$) that would result in stable fault sliding or an aseismic fault creep. If frictional strength decreases, it indicates a velocity-weakening behavior (a-$b < 0$), which is pre-requisite for unstable, stick-slip behavior associated with earthquake nucleation. The friction rate parameter (a-b) with shear strain of the reference material is shown in Fig. 5c. The constitutive parameter (a-b) for F110 undergoes a transition from positive to negative and evolves with shear strain - agreeing with previous studies.[18,21] Under our experimental conditions, this critical shear strain that is required to develop unstable slip is ~3.5, and is explained by the shear localization zone formed at this specific displacement. Finally, we compared our steady state frictional strengths with those reported in the literature (Fig. 5d). It is apparent that our values are in the range of previous studies, validating the apparatus.

3.4. Concurrent measurement of frictional and hydraulic properties

The mini-DDS is specifically designed for the rapid and simultaneous measurement of frictional properties and permeability. To identify the independence and reproducibility of the concurrent measurements we first measure permeability of F110 under static non-shearing conditions before extending to concurrent measurements.

3.4.1. Permeability measurement

Permeability is measured under a constant effective stress, as before, but for null shearing velocity in the same configuration of Fig. 1a. During a test a constant pressure difference (ΔP) is applied between the upstream (P_p) and the downstream reservoir (atmosphere pressure), with a magnitude of $\Delta P = P_p$. Permeability (y) can be recovered once flow reaches steady state (q_c = constant) from Darcy's Law, with uncertainty given by noise and small fluctuations in flow rate.

$$q_c = -\frac{kA}{\mu}\frac{\Delta p}{L_e} \tag{8}$$

where q is the volumetric flow rate [m^3/s], k is the permeability [m^2] of gouge in the direction of shear, μ is dynamic viscosity of the fluid (1.12×10^{-3} Pa s for water) and Δp [Pa] is the differential between upstream and downstream reservoir pressures. L_e is the effective length of the sample. For a null shearing velocity permeability test where the effective length of the sample remains constant. For permeability measurement concurrently with frictional properties, where samples are elongating and thinning with slip, this value can be calculated from the initial length and subtracting the load point displacement (Fig. 1b). A is the slip dependent cross-sectional area of the sample, which is defined as the product of gouge width (w) and thickness (h). The gouge thickness is evaluated by the volume change of the confining fluid as:

$$h = h_0 - \alpha \times \frac{\int_{t_0}^{t} q_c dt}{w * L_e} \tag{9}$$

where h_0 is initial thickness, $q_c$is the confining fluid influx. Since this flux is not only influenced by gouge dilation/compaction, but also evolves within the core configuration system (jacket deformation, putty compression, etc.), a correction coefficient (α) is applied. When the experiment is completed, we remove the sample and measure the final

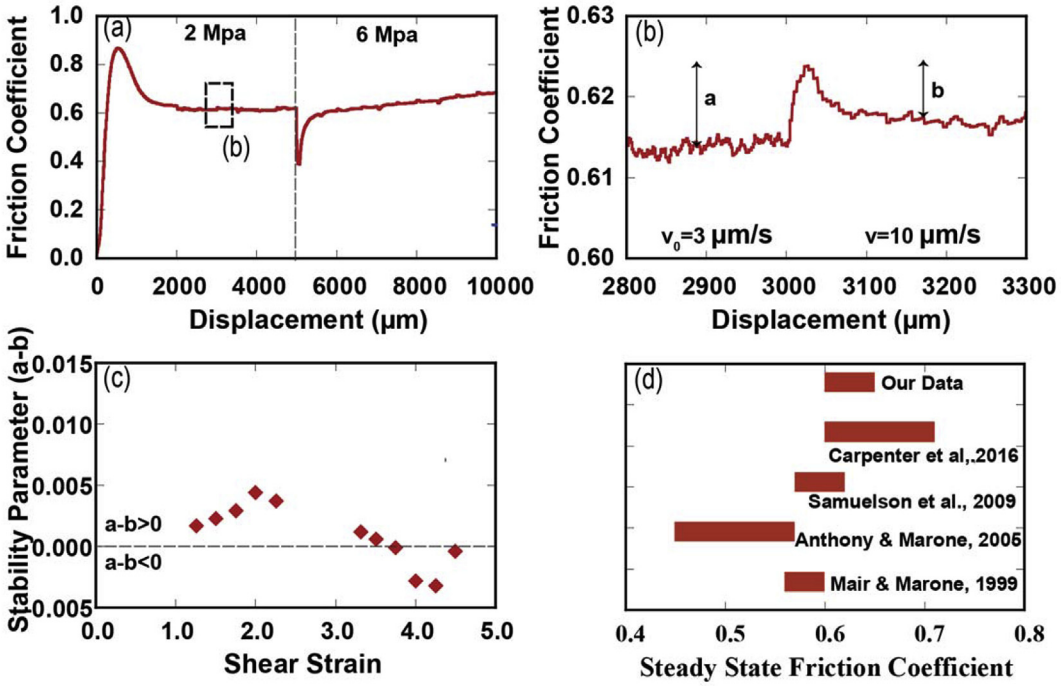

Fig. 5. Frictional properties: (a) Displacement versus friction for F110 (Exp. No.10). (b) Zoom-in of the dotted box in (a), showing the velocity-stepping (VS) direct effect, a, and evolution effect, b. (c) Friction constitutive parameters of the F110. (d) Comparison of our steady state friction values to those within the literature.

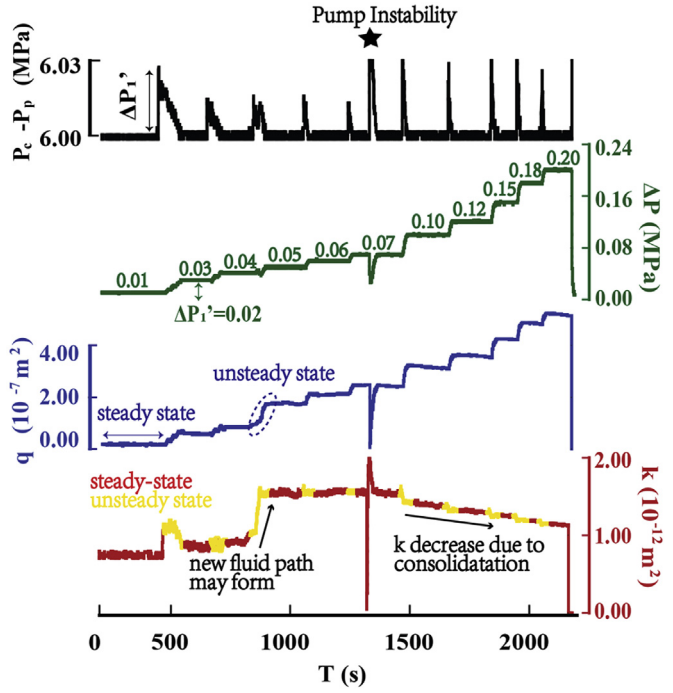

Fig. 6. A series of permeability tests is completed with a stepped increase in pressure difference (Δ*P*) to determine the optimum value of pressure difference for the concurrent measurement of frictional properties and permeability. A constant effective stress of 6 MPa is maintained by increasing (ΔP_i') as the confining pressure is incremented. Constant pressure difference is applied for each step (green) of the test with transition from one steady state to the next. Permeability (*k*) is then recovered from Darcy's Law once flow reaches a steady state (red). During experiments, pump instability may occur unexpectedly (labeled by star) where the pump shuts down for a few seconds, resulting in sudden decrease in pressure difference, flow rate and therefore inferred permeability. (For interpretation of the references to colour in this figure legend, the reader is referred to the Web version of this article.)

sample thickness (h). With all other parameters in eqn. (9) recorded, $\alpha$is then evaluated, Finally, the fault-parallel permeability of the sample is recovered.

We measure permeability continuously as pressure difference is incremented under constant confining stress of 6 MPa. For each step, flow rate stabilizes as the sample saturates with steady state reached > 200 s as the confining pressure is incremented ($\Delta p_i'$) to compensate for the small interior fluid pressure within the sample. Permeability can be calculated by assuming steady state flow and in using Darcy's Law, with steady state shown in red and transitional regimes in yellow (Fig. 6).

If the tested material is rigid, homogenous and isotropic, the permeability will be insensitive to effective stress – this is not the case for gouge. For example, the permeability of the reference gouge varies between 0.8 and 1.5×10^{-12} m^2 with a pressure difference of 0.01–0.24 MPa as shown in Fig. 6. The initail permeability is 0.8×10^{-12} m,[2] and slightly increases over the first three steps of increased pressure difference. At ~800s, permeability suddenly increases by 50% and then remains constant for the next few pressure increments, possibly indicating that a new fluid flow path is being established and stabilized. After 1500s, the permeability imperceptibly decreases until the conclusion of the experiment, which may result from the consolidation of the gouge due to a series of effective stress spikes as the confining and fluid pressures are offset. We also observe a time-dependent decline in permeability > 1500s, where pore pressure over each step is constant while flow rate declines. This is suspected to be a result of pressure solution/compaction resulting in permeability reduction [14].

Maintaining both confining and pore pressures constant during experiments limits the impact on permeability from friction/shearing response. Thus, in the further concurrent measurement of frictional properties and permeability, constant effective stress is applied and permeability is then recovered from the assumed steady state with a constant pressure difference of 30 kPa. In this condition, flow rate is sufficiently low to limit the mobilization of fines and prevent local increases in porosity and permeability. In addition, applying a relatively low pressure difference limits the frequency of refilling pumps during the experiment that result in discontinuous recording of friction-permeability.

3.4.2. Concurrent measurements of friction and permeability

We conduct two identical experiments to examine the reproducibility and robustness of the frictional and hydraulic properties recovered from shearing F110 at a confining stress of 5 MPa. We first fluid saturates the sample with de-ionized water (Pump C, constant upstream pressure) and initiate shear at a prescribed loading rate of 10 μm/s until steady friction is reached (peak shear stress). The sample is then subjected to a series of load point velocity-stepping experiments, followed by a slide-hold-slide (SHS) sequence with hold times of 100s, 300s, 500s, and 1000s. (Fig. 7a). The reliability and reproducibility of the apparatus is verified from the virtual overlap in the response curves for the evolution of friction coefficient and permeability. The frictional constitutive parameter (*a-b*) is evaluated and compared with that measured under dry conditions (Fig. 7b). This shows that the (*a-b*) stability coefficient of F110 when water saturated is overall higher than that when dry and it is expected to shear localize only at larger shear strains. During the SHS sequence, $\triangle\mu$ is defined as the relative change in static friction and $\triangle\mu_c$ as relaxation creep, as illustrated in Fig. 7c. Data from these two identical experiments show that the frictional healing rate increases with the duration of loading (Fig. 7d). The average healing rate is 0.013s^{-1}, which is close to that reported in the literature.[22–24]

The evolution of permeability is monitored during the experiment and fluctuates around $\sim 1.2 \times 10^{-12}$ m^2 after the running-in of shear displacement (Fig. 8). In the first few velocity steps, there is a clear trend that permeability enhances as velocity increases and declines as velocity decreases. This can be explained by shear induced dilation due to velocity increases and compaction due to velocity drops, which is consistent with previous studies.[21,25] At later velocity steps, permeability declines even if gouge continuously undergoes dilation during up-stepping (7000–10000 μm). This is because the effects of shear-induced grain degradation and wear products become more dominant as shear displacement accumulates and their rearrangement reduces permeability by nearly 33%. Additionally, dilatancy decreases with shear displacement due to geometric thinning of the gouge layers, which results in much less permeability enhancement than over previous velocity jumps.

Shear stress, velocity change and permeability evolution of SHS experiments are zoomed-in and shown in Fig. 9. Shear stress declines during the holds then sharply increases to a peak during reactivation, before restabilizing at steady state friction. The magnitude of the peak stress increases with the increased duration of the prior hold period, representing time-dependent frictional healing, consistent with previous studies.[12] After successive holds of increasing duration, peak strength decreases due to shear stress relaxation during holds and offsets the effects of subsequent frictional healing. In general, permeability increases during holds and decreases during sliding. This is possibly because wear products are generated and accumulate in the pore space that decrease the permeability while sliding. During the hold period, shear stress is released and wear products are less produced. Additionally, unclogging by fluid flow flushing of wear products results in the observed permeability enhancement. We observe that permeability slightly decreases during the first 100s hold, which is opposite to the permeability trend of holds on other samples. This could possibly

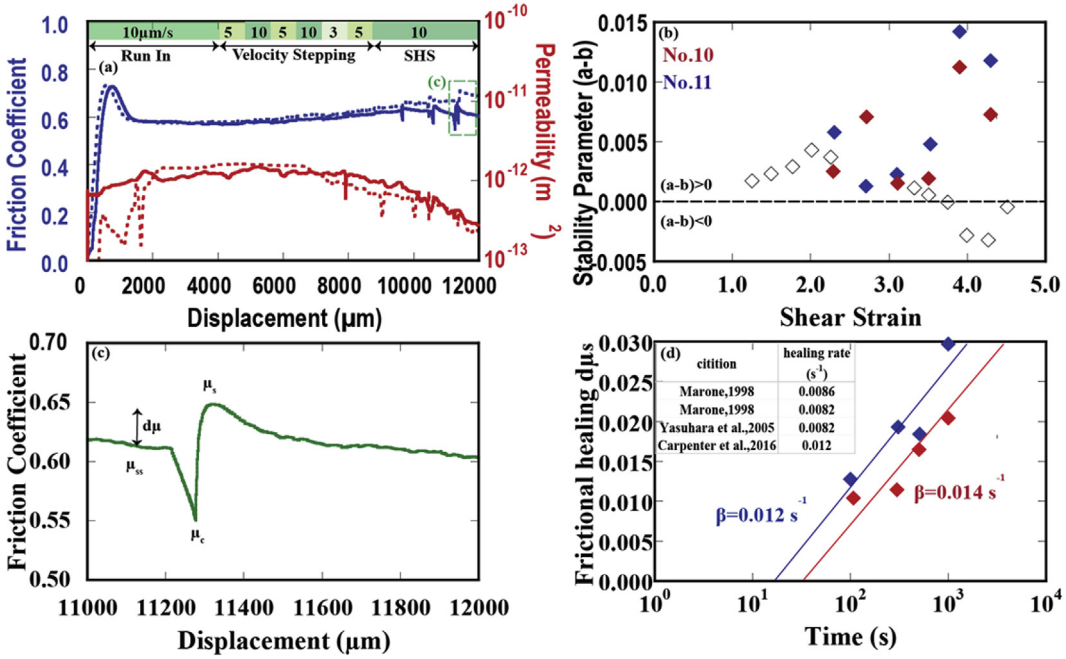

Fig. 7. Two identical experiments to measure frictional and hydraulic properties of F110 (Exp.No.10,11): (a) Evaluation of friction coefficient and permeability evolution (log scale) of F110. (b) Constitutive parameters of F110 when water saturated compared to that (No.10,11) with when dry (No.9). (c) Illustrative figure defines friction healing and creep (d) Frictional healing rate of F110 compared to previous studies.

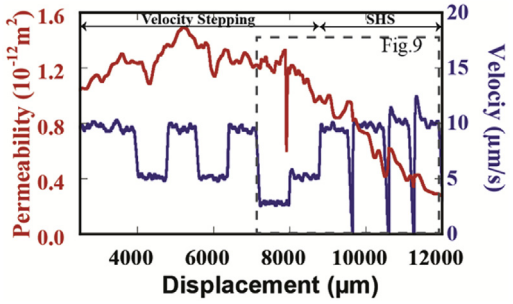

Fig. 8. Evaluation of friction coefficient and permeability evolution of F110 during VS and SHS (No.10).

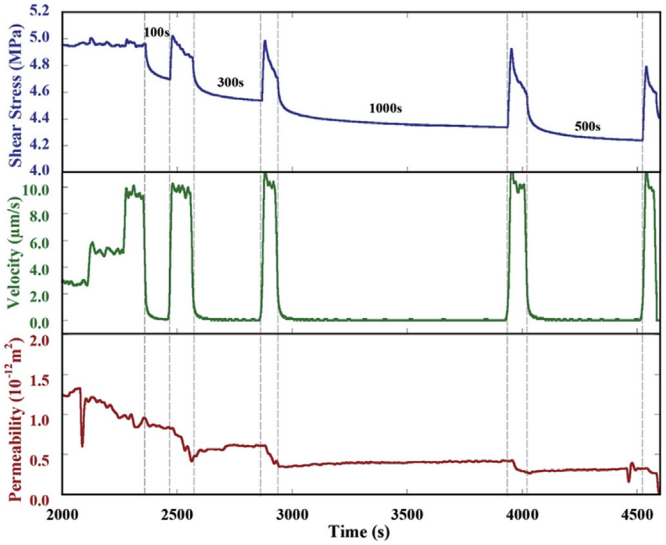

Fig. 9. Zoom-in view of Fig. 8: Shear stress, velocity and permeability change during SHS (No.11).

happen when accumulated wear products generated by previous sliding have not been fully flushed by water flow within such a short time as 100s. Permeability during the hold does not show time-dependent decline probably because we did not hold for sufficiently long (> 1500s) in the SHS test and that permeability evolution is mainly dominated by the effects of unclogging.

4. Discussion

We describe the assembly, experimental procedure and response of the mini-DDS apparatus for the concurrent measurement of friction, stability and shear parallel permeability on analog fault gouge. The assembly allows the DDS to be deployed within a traditional cylindrical standard-triaxial core holder such as a TEMCO enabling coupled frictional-stability-permeability experiments to be completed with ease, rapidity and precision. Different form other devices, our mini-DDS is capable of conducting extended duration experiments (time scale order of months) to explore the long-term rheological and permeability behavior, representative of inter-seismic repose, without consuming significant resources. Additionally, the DDS is highly compatible for expansions such as dilation/compaction monitoring using sample mounted strain gages, active ultrasonic mapping of fracture propagation and passive acoustic emission of micro earthquakes. The setup is also capable of injecting high pressure or chemically reactive fluids to investigate fault response to abrupt reactivation and geo-chemical reactions.

Despite thorough calibrations for jacket resistance, experiments at high confining pressure (greater than 10 MPa), and gouge samples with large grain sizes (greater than 200 μm) are difficult to accomplish. Additionally, in the current configuration, the shear loading direction is aligned to that of fluid flow, and flow-back occurs when the shear platen invades the fluid-filled supporting base. This effect may be calibrated out by compensating for this reflux – evaluating this from the product of shear velocity and cross-sectional area of the platen as the volume rate incursion of the platen intrusion. This makes permeability measurement problematic where the magnitude of this calibrated flow-back is greater than the measured Darcy flow rate across the sample i.e.

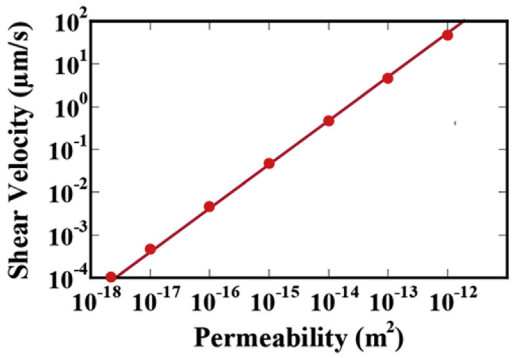

Fig. 10. Maximum shear velocities that allow the accurate measurement of permeability considering flow-back.

where a low-permeability sample is sheared at a relatively high velocity. Thus, if we consider permeability is determined with sufficient accuracy when flow back is 1/10 of the measured flow rate, we present the maximum shear velocities for a range of permeabilities from the lowest measurable value ($2.2 \times 10^{-18}\,m^2$) to $10^{-12}\,m^2$ as shown in Fig. 10. It is apparent that shear velocity has to be lower than 10^{-4} μm/s when we shear a low-permeability sample so that permeability can be measured accurately. If the sample is of high-permeability (i.e. $10^{-12}\,m^2$), its permeability can be precisely measured with shear velocity even as fast as 48 μm/s. Therefore, we suggest choosing a suitable shear velocity to concurrently measure the frictional property and permeability based on Fig. 10.

5. Conclusions

A novel miniature double direct shear (mini-DDS) apparatus has been designed and assembled within a standard TEMCO pressure vessel, to concurrently measure the evolution of frictional strength, stability, healing and along-fault permeability under *in situ* stresses and temperatures.

The mini-DDS is capable of conducting long-term experiments at a high resolution with comparable samples to conventional DDS setups and is flexible to future expansions, such as dilation/compaction monitoring using sample-mounted strain gauges; acoustic mapping of micro fracture propagation and its impact on permeability; and injecting high-pressure or reactive fluids to investigate the corresponding evolution of frictional and transport properties.

System stiffness is carefully calibrated as 0.067 kN/μm. Jacket resistance and confining stress are positively correlated. System reliability is validated via reference materials, including F110, which are consistent with those reported in the literature.

At early stages of deformation, shear velocity change induced dilation/compaction dominates permeability evolution: permeability enhances as velocity increases and declines as velocity decreases. As shear displacement accumulates, grain comminution becomes a more dominant mechanism with the generation of wear products causing permeability decreases during slip by clogging the fluid channels. During hold periods, unclogging occurs by fluid flow flushing of wear products and results in permeability enhancement.

High confining stress (greater than a 10 MPa ceiling, depending on the penetration resistance of the jacket) and low shear loading rates, due to the mandatory compensation of shear extrusion, are current limitations of the mini-DDS apparatus.

Acknowledgements

This work is a partial result of support provided by DOE Grant DE-FE0023354 and the DOE EGS Collab. This support is gratefully acknowledged.

References

1. Rice JR. Heating and weakening of faults during earthquake slip. *J Geophys Res Solid Earth.* 2006;111(5) https://doi.org/10.1029/2005JB004006.
2. SIBSON RH. Interactions between temperature and pore-fluid pressure during earthquake faulting and a mechanism for partial or total stress relief. *Nat Phys Sci.* 2013;243(126):66–68. https://doi.org/10.1038/physci243066a0.
3. Andrews DJ. A fault constitutive relation accounting for thermal pressurization of pore fluid. *J Geophys Res Solid Earth.* 2003;107(B12) https://doi.org/10.1029/2002jb001942 ESE 15-1-ESE 15-8.
4. Ellsworth WL. Injection-induced earthquakes. *Science.* 2013;341(July):1–8. https://doi.org/10.1785/gssrl.83.2.250 80-.
5. Shapiro SA, Dinske C, Rothert E. Hydraulic-fracturing controlled dynamics of microseismic clouds. *Geophys Res Lett.* 2006;33(14):1–5. https://doi.org/10.1029/2006GL026365.
6. Zoback MD, Gorelick SM. Earthquake triggering and large-scale geologic storage of carbon dioxide. *Proc Natl Acad Sci U S A.* 2012;109(26):10164–10168. https://doi.org/10.1073/pnas.1202473109.
7. Zoback MD, Kohli A, Das I, McClure MW. The importance of slow slip on faults during hydraulic fracturing stimulation of shale gas reservoirs. *SPE Am Unconv Resour Conf.* 2012;2011. https://doi.org/10.2118/155476-MS.
8. Walsh FR, Zoback MD. Oklahoma's recent earthquakes and saltwater disposal. *Sci Adv.* 2015;1(5) https://doi.org/10.1126/sciadv.1500195.
9. Majer EL, Baria R, Stark M, et al. Induced seismicity associated with enhanced geothermal systems. *Geothermics.* 2007;36(3):185–222. https://doi.org/10.1016/j.geothermics.2007.03.003.
10. Gaucher E, Schoenball M, Heidbach O, et al. Induced seismicity in geothermal reservoirs: a review of forecasting approaches. *Renew Sustain Energy Rev.* 2015;52:1473–1490. https://doi.org/10.1016/j.rser.2015.08.026.
11. Dieterich JH, Kilgore BD. Imaging surface contacts: power law contact distributions and contact stresses in quartz, calcite, glass and acrylic plastic. *Tectonophysics.* 1996;256(1-4):219–239. https://doi.org/10.1016/0040-1951(95)00165-4.
12. Marone C. Laboratory-derived friction laws and their application to seismic faulting. *Annu Rev Earth Planet Sci.* 1998;26(1):643–696. https://doi.org/10.1146/annurev.earth.26.1.643.
13. Fang Y, Elsworth D, Wang C, Ishibashi T, Fitts JP. Frictional stability-permeability relationships for fractures in shales. *J Geophys Res Solid Earth.* 2017;122(3):1760–1776. https://doi.org/10.1002/2016JB013435.
14. Im K, Elsworth D, Fang Y. The influence of preslip sealing on the permeability evolution of fractures and faults. *Geophys Res Lett.* 2018;45(1):166–175. https://doi.org/10.1002/2017GL076216.
15. Crawford BR, Faulkner DR, Rutter EH. Strength, porosity, and permeability development during hydrostatic and shear loading of synthetic quartz-clay fault gouge. *J Geophys Res Solid Earth.* 2008;113(3):1–14. https://doi.org/10.1029/2006JB004634.
16. Kaproth BM, Kacewicz M, Muhuri S, Marone C. Permeability and frictional properties of halite-clay-quartz faults in marine-sediment: the role of compaction and shear. *Mar Pet Geol.* 2016;78:222–235. https://doi.org/10.1016/j.marpetgeo.2016.09.011.
17. Faoro I, Niemeijer A, Marone C, Elsworth D. Influence of shear and deviatoric stress on the evolution of permeability in fractured rock. *J Geophys Res Solid Earth.* 2009;114(1):1–10. https://doi.org/10.1029/2007JB005372.
18. Samuelson J, Elsworth D, Marone C. Shear-induced dilatancy of fluid-saturated faults: experiment and theory. *J Geophys Res Solid Earth.* 2009;114(12):1–15. https://doi.org/10.1029/2008JB006273.
19. Collettini C, Di Stefano G, Carpenter B, et al. A novel and versatile apparatus for brittle rock deformation. *Int J Rock Mech Min Sci.* 2014;66:114–123. https://doi.org/10.1016/j.ijrmms.2013.12.005.
20. Giorgetti C, Collettini C, Scuderi MM, Barchi MR, Tesei T. Fault geometry and mechanics of marly carbonate multilayers: an integrated field and laboratory study from the Northern Apennines, Italy. *J Struct Geol.* 2016;93:1–16. https://doi.org/10.1016/j.jsg.2016.10.001.
21. Mair K, Marone C. Friction of simulated fault gouge for a wide range of velocities and normal stresses. *J Geophys Res Solid Earth.* 1999;104(B12):28899–28914. https://doi.org/10.1029/1999JB900279.
22. Marone C. The effect of loading rate on static friction and the rate of fault healing during the earthquake cycle. *Nature.* 1998;391(6):69–72. https://doi.org/10.1038/nature34157.
23. Yasuhara H, Marone C, Elsworth D. Fault zone restrengthening and frictional healing: the role of pressure solution. *J Geophys Res Solid Earth.* 2005;110(6):1–11. https://doi.org/10.1029/2004JB003327.
24. Carpenter BM, Ikari MJ, Marone C. *Laboratory Observations of Time-dependent Frictional Strengthening and Stress Relaxation in Natural and Synthetic Fault Gouges.* 2016; 2016:1183–1201. https://doi.org/10.1002/2015JB012136 Received.
25. Candela T, Brodsky EE, Marone C, Elsworth D. Laboratory evidence for particle mobilization as a mechanism for permeability enhancement via dynamic stressing. *Earth Planet Sci Lett.* 2014;392:279–291. https://doi.org/10.1016/j.epsl.2014.02.025.